Geophysical Journal International

Geophys. J. Int. (2013) **195,** 342–351
Advance Access publication 2013 August 7

doi: 10.1093/gji/ggt259

Measurements of seismic attenuation and transient fluid pressure in partially saturated Berea sandstone: evidence of fluid flow on the mesoscopic scale

Nicola Tisato[1] and Beatriz Quintal[2,*]

[1]*Department of Earth Sciences, ETH Zurich, Sonneggstrasse 5, NO E3, 8092 Zurich, Switzerland. E-mail: nicola.tisato@erdw.ethz.ch*
[2]*Department of Earth Sciences, ETH Zurich, Sonneggstrasse 5, NO E61, 8092 Zurich, Switzerland*

Accepted 2013 July 1. Received 2013 May 12; in original form 2013 February 12

SUMMARY

A novel laboratory technique is proposed to investigate wave-induced fluid flow on the mesoscopic scale as a mechanism for seismic attenuation in partially saturated rocks. This technique combines measurements of seismic attenuation in the frequency range from 1 to 100 Hz with measurements of transient fluid pressure as a response of a step stress applied on top of the sample. We used a Berea sandstone sample partially saturated with water. The laboratory results suggest that wave-induced fluid flow on the mesoscopic scale is dominant in partially saturated samples. A 3-D numerical model representing the sample was used to verify the experimental results. Biot's equations of consolidation were solved with the finite-element method. Wave-induced fluid flow on the mesoscopic scale was the only attenuation mechanism accounted for in the numerical solution. The numerically calculated transient fluid pressure reproduced the laboratory data. Moreover, the numerically calculated attenuation, superposed to the frequency-independent matrix anelasticity, reproduced the attenuation measured in the laboratory in the partially saturated sample. This experimental—numerical fit demonstrates that wave-induced fluid flow on the mesoscopic scale and matrix anelasticity are the dominant mechanisms for seismic attenuation in partially saturated Berea sandstone.

Key words: Numerical solutions; Creep and deformation; Elasticity and anelasticity; Seismic attenuation; Acoustic properties.

INTRODUCTION

Ideally, seismic wave attenuation calculated from field data could be useful to estimate fluid content and saturation in subsurface fluid–rock systems. These fluid–rock systems can be hydrocarbon reservoirs, geologically sequestered carbon dioxide reservoirs, nuclear waste repositories or even subsurface domains where partially molten rocks or rocks and fluids coexist (Mitchell & Romanowicz 1999).

Experimental studies show that rock samples saturated with fluids exhibit higher and frequency-dependent attenuation than dry samples (Spencer 1981; Paffenholz & Burkhardt 1989; Batzle *et al.* 2006; Tisato & Madonna 2012; Madonna & Tisato 2013). However, the physical mechanisms dominating seismic attenuation in fluid-saturated rocks remain to be identified.

In this study, we performed laboratory experiments using the broad-band attenuation vessel (BBAV) designed to measure attenuation at seismic frequencies (0.1–100 Hz, Tisato & Madonna 2012). We also measured the transient fluid pressure caused by a quick variation of the compressional stress applied on top of the sample. The transient fluid pressure was measured at different positions in the fluid-saturated rock sample. The pressure sensors were introduced into the sample and recorded pressure variations in a fraction of a millisecond. Measurements of transient fluid pressure are related to fluid flow on the mesoscopic scale, which is a scale much larger than the pore size and much smaller than seismic wavelengths. Our main objective was to verify whether wave-induced flow of fluid on the mesoscopic scale may explain the high amplitudes and the frequency dependence of the measured seismic attenuation. For this purpose, we computed attenuation and fluid pressure associated with this attenuation mechanism.

Wave-induced fluid flow on the mesoscopic scale is a physical mechanism that may yield significant attenuation at seismic frequencies in partially saturated porous media (Pride *et al.* 2004). The passing seismic wave induces fluid pressure differences between regions of different compliances. The resulting pressure gradients induce fluid to flow and, therefore, part of the energy involved in the wave propagation is lost due to viscous dissipation. In partially saturated rocks, regions having different compliances are

* Now at: Applied and Environmental Geophysics Group, University of Lausanne, Quartier UNIL—Mouline, Géopolis, Bureau 3159, 1015 Lausanne, Switzerland.

due to heterogeneities in fluid saturation, accompanied or not by heterogeneities in the solid frame. In White's model, a partially saturated rock is approximated by a medium having a homogeneous solid frame and mesocopic-scale heterogeneities fully saturated with one fluid and the background fully saturated with another fluid, the so-called patchy saturation (White 1975).

Dutta & Odé (1979a,b) showed that patchy saturation could be simulated using Biot's equations of wave propagation in poroelastic media (Biot 1962) with spatially varying petrophysical parameters. Methodologies computationally efficient in calculating attenuation due to wave-induced fluid flow on the mesoscopic scale have been recently proposed (Masson & Pride 2007; Rubino *et al.* 2009; Wenzlau *et al.* 2010; Quintal *et al.* 2011). These methods are based on quasi-static tests performed on poroelastic models. Quintal *et al.* (2011) proposed to solve Biot's equations (1941) for consolidation of poroelastic media for such tests, rather than Biot's equations (1962) of wave propagation, as previously done. We followed this methodology to compute attenuation due to wave-induced fluid flow on the mesoscopic scale in 3-D numerical models.

We first summarize the techniques employed for laboratory measurements and for numerical modelling. Then, we present laboratory measurements of attenuation and transient fluid pressure in Berea sandstone in four saturation conditions (dry, 62.4, 86.6 and 97.1 per cent water). Measurements for dry conditions are useful to estimate the matrix anelasticity. Finally, we present numerical results for attenuation and fluid pressure for a model representing the sample saturated with 97.1 per cent water, and compare with laboratory measurements.

Combining measurements of attenuation and fluid pressure, and using numerical modelling to assist in the data interpretation, allowed concluding that the amplitude and frequency dependence of seismic attenuation in partially saturated Berea sandstone can be explained by wave-induced fluid flow on the mesoscopic scale if the matrix anelasticity is taken into account.

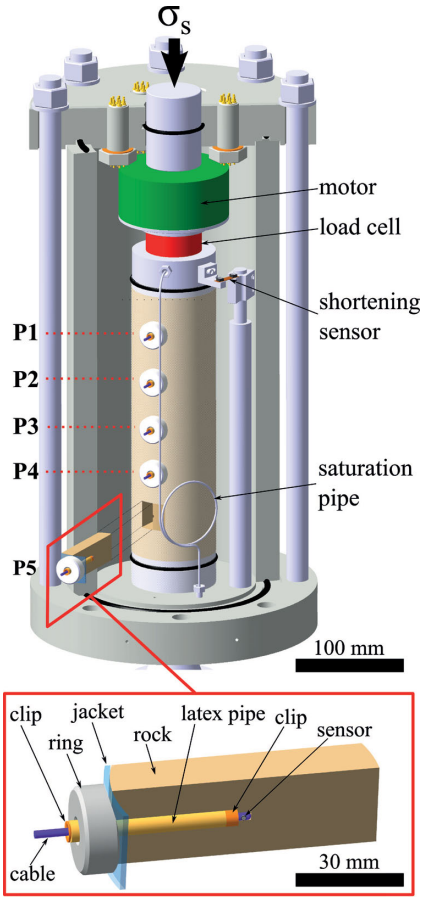

Figure 1. Sketch of the BBAV (Tisato & Madonna 2012). Transient fluid pressure (P1, P2, P3, P4 and P5) is measured at five points vertically distributed along the sample. The inset shows how the pore pressure sensors are placed in the sample.

MATERIAL AND METHODS

Laboratory measurements

Sample description and saturation

The cylindrical rock sample is 7.6 cm in diameter and 25.0 cm in length. Its petrophysical properties are listed in Table 1. We use the same BS001 Berea sandstone sample employed by Tisato & Madonna (2012). Madonna *et al.* (2012) showed that this rock can be considered homogeneous and isotropic.

The cylindrical sample is placed vertically in the BBAV (Fig. 1). Water saturation is increased from about 0 per cent to almost 100 per cent by injecting water at the bottom using a pump connected to the pore fluid circuit. For 97.1 per cent water saturation, the injection was one order of magnitude more time consuming (it lasted about 20 hr) than for lower saturations (about 1–2 hr). Longer injection might have promoted the migration of air from the bottom to the top of the sample. Saturation is calculated according to the rock porosity and the volume of water injected into the sample. This volume is estimated using graduated burettes connected to the pump. The sample is left at rest for few hours between the saturation procedure and the measurements. Both the attenuation and fluid pressure tests were conducted under undrained conditions (valves of the pore fluid circuit were closed). A detailed description of sample sealing is given in Appendix A.

Table 1. Physical properties of the solid frame of the rock sample (e.g. Wang 2000).

Rock sample	Berea sandstone
Density of the grains (kg m^{-3})	2650
Bulk modulus of the grains (GPa)	36
Porosity (per cent)	20
Permeability (mD)	300
Bulk modulus of the dry frame (GPa)	7
Shear modulus of the dry frame (GPa)	4.8

Attenuation measurements

We measured seismic attenuation in a partially saturated rock sample for frequencies ranging from 1 to 100 Hz. The BBAV was calibrated according to Tisato & Madonna (2012), and it employs the subresonance method (McKavanagh & Stacey 1974). A sinusoidal compressive normal stress is applied vertically on top of the sample and the resulting sinusoidal vertical strain is measured. Subsequently, the phase shift φ between the applied stress and the resulting stain is calculated (Nowick & Berry 1972). The attenuation (Q^{-1}) can be calculated as:

$$Q^{-1} = \tan(\varphi), \quad (1)$$

where Q is the quality factor. Attenuation is in extensional mode and is related to the complex Young's modulus (E) as:

$$Q^{-1} = \frac{\mathrm{Im}(E)}{\mathrm{Re}(E)} \tag{2}$$

(e.g. Carcione 2007), where Im and Re denote the imaginary and real parts, respectively. Using the data for applied stress and resulting strain, we can calculate the real part of the Young's modulus:

$$\mathrm{Re}(E) = \frac{\sigma_{\max}}{\varepsilon_{\max}} \cos(\varphi), \tag{3}$$

where $\sigma_{\max}$ and $\varepsilon_{\max}$ are the maximal amplitudes of the sinusoidal vertical stress and strain, respectively (Lakes 2009).

Fluid pressure measurements

The BBAV was also used to measure transient fluid pressure in the partially saturated sample. The transient fluid pressure was caused by a quick variation of the compressional stress applied on top of the sample, which was an approximate step function. Five pressure sensors, vertically spaced about 4.2 cm, were laterally introduced into the sample (Fig. 1). Each sensor was introduced through a horizontal hole drilled to the symmetry axis of the cylindrical sample. We used an inflatable latex pipe between the sensor cable and the inner wall of the holes to seal them and avoid introducing a significant amount of artificial porosity. More detailed technical information about the sensors, their placement and sealing is given in Appendix B.

Experimental conditions

A confining pressure, P_c, was applied on the sample during both attenuation and fluid pressure experiments. A compressive normal stress consisting of a constant static part, σ_s and a transient part, σ_t, was applied on top of the sample. The static stress σ_s was applied to keep the top and bottom surfaces of the sample adherent to the sample holders. The transient stress σ_t behaves as sinus function in the attenuation experiments and as an approximate step function in the fluid pressure experiments. In the latter, σ_t was applied in less than 10 ms using a piezoelectric motor to generate a quick variation of vertical stress (Fig. 1). Transient σ_t caused a transient vertical strain ε_t and a transient fluid pressure, P_f. The state of stress on the sample can be summarized as follows: $\sigma_1 = P_c + \sigma_s + \sigma_t$ and $\sigma_2 = \sigma_3 = P_c$, where σ_1, σ_2 and σ_3 are the principal stresses, with σ_1 vertical. The magnitudes or limits of the parameters used for this work are given in Table 2.

We measured attenuation and fluid pressure in the Berea sandstone sample at room temperature and approximately room pressure (P_c in Table 2).

Table 2. Strain and stress conditions for the attenuation and fluid pressure experiments.

Experiment	Attenuation	Fluid pressure
P_c (MPa)	0.25	0.25
σ_s (MPa)	1.1	1.1
σ_t (MPa)	Up to 0.012	Up to 0.12
ε_1	Within $[1, 2] \times 10^{-6}$	Within $[1, 2] \times 10^{-5}$
P_f (MPa)	At least 0.1	At least 0.1

Numerical modelling

The numerical methodology proposed by Quintal *et al.* (2011) was used to compute attenuation due to wave-induced fluid flow on the mesoscopic scale. Quasi-static creep tests were performed on poroelastic models by solving Biot's equations for the consolidation of poroelastic media (Biot 1941). These equations were used in the displacement–pressure formulation and solved with the finite-element method (Zienkiewicz *et al.* 1999). An undrained boundary condition is mathematically fulfilled (natural boundary condition), which is possible due to the displacement–pressure formulation (e.g. eq. B7 in Quintal *et al.* 2011). The algorithm was validated through comparison of numerical results with analytical solutions. To solve our problem for a 3-D model, we used the finite-element commercial software COMSOL Multiphysics (Zurich, Switzerland). We employed an unstructured mesh composed of tetrahedral elements.

To compare numerical results with laboratory data, we performed simulations on a cylindrical numerical model representing an idealized version of the rock sample. The applied boundary conditions were:

(1) An approximate step stress (as function of time) applied on top of the cylinder.
(2) A fixed bottom, that is, no displacement in the z (vertical) direction.
(3) The sides are also fixed, that is, there is no displacement in the x and y directions.

Time-dependent normal total stress and strain in the z direction, σ_{zz} and ε_{zz}, respectively, were obtained from the numerical experiment. Subsequently a first-order time derivative was applied resulting in the rates $\dot{\sigma}_{zz}$ and $\dot{\varepsilon}_{zz}$. The stress and strain rates were then converted into the frequency domain by using a fast Fourier transform, resulting in $\hat{\sigma}_{zz}$ and $\hat{\varepsilon}_{zz}$. The complex and frequency-dependent P-wave modulus was calculated as:

$$H(\omega) = \frac{\hat{\sigma}_{zz}}{\hat{\varepsilon}_{zz}}, \tag{4}$$

where ω is the angular frequency ($=2\pi f$). The complex and frequency-dependent Young's modulus is calculated as

$$E(\omega) = \frac{\mu(3H - 4\mu)}{H - \mu}, \tag{5}$$

where H was obtained with eq. (4), and μ is the shear modulus of the saturated medium. The attenuation in extensional model can then be calculated using eq. (2).

Since Berea sandstone has a homogeneous solid frame at mesoscopic scales (Madonna *et al.* 2012), only heterogeneities in fluid saturation were implemented in the numerical model. According to Gassmann's equations, when the solid frame is homogeneous the shear modulus of the saturated medium (used in eq. 5) is equal to the shear modulus of the dry frame (Gassmann 1951; Berryman 1999). The properties used for the solid frame and for the fluids, water and air, are listed in Tables 1 and 3. These properties are given for the conditions at which the laboratory experiments were performed.

Table 3. Physical properties of the fluids.

Fluid	Water	Air
Density of the fluid (kg m^{-3})	1000	1
Viscosity of the fluid (Pa s)	0.001	2×10^{-5}
Bulk modulus of the fluid (GPa)	2.2	10^{-4}

RESULTS

Laboratory experiments

The saturation degrees in the Berea sandstone sample were dry (i.e. 0 per cent), 62.4% (±1.8%), 86.6% (±2.4%) and 97.1% (±2.7%) water. Attenuation measurements in extensional mode for these four saturation degrees are shown in Fig. 2.

For the dry sample, Q^{-1} is approximately constant, while Re(E) increases from about 11.6 to 12 GPa in the bandwidth 1–100 Hz. These results are in agreement with the nearly constant Q^{-1} model (Liu *et al.* 1976) that predicts a constant Q^{-1} and a linear increase of Re(E) in the logarithmic frequency scale. Measurements for Q^{-1} and Re(E) for the partially saturated samples (with 62.4, 86.6 and 97.1 per cent water) are also shown in Fig. 2. In these cases, Q^{-1} exhibits a frequency-dependent behaviour, in contrast to Q^{-1} for the dry sample.

Transient fluid pressure, caused by a step stress applied on top of the sample, was also measured for these four saturation degrees (Fig. 3). In general, we observe that the higher the water saturation, the greater the fluid pressure. The fluid pressure for the dry sample is constant and approximately zero. For the partially saturated samples, the fluid pressure varies significantly with time and, immediately after the quick variation of stress ($t \rightarrow 0$), it is higher at the bottom of the sample. This suggests that water saturation is also higher at the bottom of the sample, which was expected because this is where water was injected. The difference in fluid pressure between two neighbour sensors (Fig. 4) induces a fluid flow from the zone of higher pressure towards the zone of lower pressure. As fluid flows ($t \rightarrow 2$ s), the fluid pressure tends to equilibrium. We observed higher attenuation for higher pressure difference (Fig. 2). This suggests that wave-induced fluid flow on the mesoscopic scale is a significant attenuation mechanism taking place in the sample saturated with 86.6 or 97.1 per cent water.

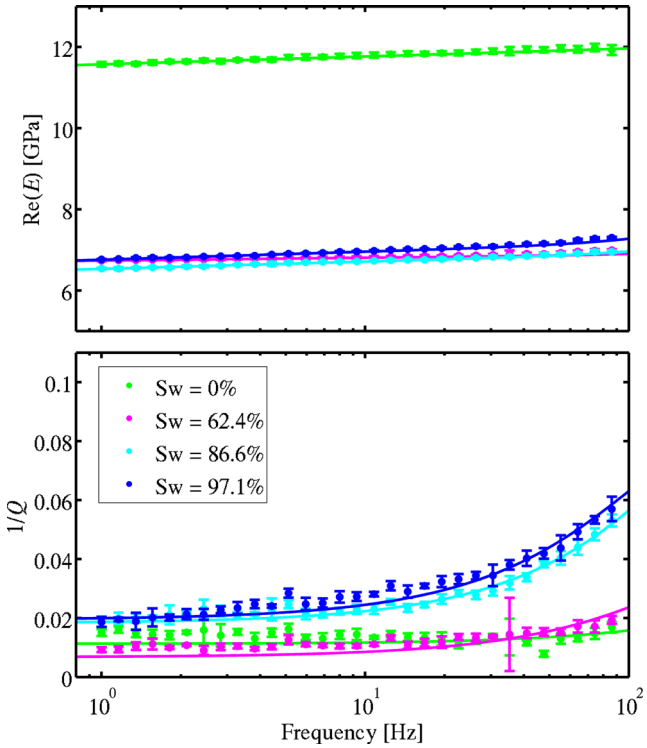

Figure 2. Laboratory measurements of the real part of Young modulus Re(E) and the related attenuation ($1/Q$) for a dry, a 62.4, 86.6 and 97.1 per cent water saturated.

Numerical experiments

The numerical model was scaled to have the same shape, dimensions and physical properties as the sample used in the laboratory. The objective was to compare numerical results and laboratory data for the case in which the rock sample contains 97.1 per cent water. For this purpose, we need a fluid distribution within the model that corresponds to the experimental case. The fluid pressure values, measured by the five sensors immediately after application of the step stress ($t \rightarrow 0$), were used to obtain the fluid distribution. At $t \rightarrow 0$, sample domains saturated with the 'incompressible' and viscous fluid (water) experienced a higher fluid pressure than air-saturated domains (Fig. 5a). This is because water has no time to migrate towards portions at lower fluid pressure (Mavko *et al.* 2009). A linear relationship between measured fluid pressure at $t \rightarrow 0$ and water saturation (Fig. 5b) is defined in a way that the total water saturation in the model is about the same as in the laboratory (97.1 per cent). Following this linear relationship, we inserted air-saturated cubic patches in a fully water saturated background to create models such as that in Fig. 5(c). Number and size of patches were increased towards the top of the model. The cubic shape was chosen because it is solved numerically using a small number of tetrahedral elements. We compared transient fluid pressure resulting from diverse models with the laboratory measurements. The model that resulted in the best agreement (Fig. 6) is the one shown in Fig. 5(c). 120 cubic patches with sides from 2.5 to 10 mm were used yielding total water saturation of approximately 98 per cent. From the same simulation as for transient fluid pressure, we recorded the resulting time-dependent normal total stress and strain in the z direction and computed attenuation (Fig. 7).

The computed attenuation is only due to wave-induced fluid flow on the mesoscopic scale. However, we observed non-negligible frequency-independent attenuation for the laboratory data of the dry sample. Such attenuation is associated with the solid frame and assumed to take place also in the measurements for the fluid-saturated sample (Johnston *et al.* 1979). To interpret laboratory data in a fluid-saturated sample, Johnston *et al.* (1979) assumed that fluid-related attenuation ($1/Q_{\mathrm{Fluid}}$) and frame-related attenuation ($1/Q_{\mathrm{Frame}}$) are independent and that the total attenuation could therefore be calculated as

$$\frac{1}{Q_{\mathrm{Total}}} = \frac{1}{Q_{\mathrm{Fluid}}} + \frac{1}{Q_{\mathrm{Frame}}}. \qquad (6)$$

We followed this assumption. The numerically calculated attenuation is taken as the value for $1/Q_{\mathrm{Fluid}}$ and the mean value of attenuation measured in the laboratory on the dry sample for $1/Q_{\mathrm{Frame}}$. The sum ($1/Q_{\mathrm{Total}}$) was compared to the laboratory measurements of attenuation in the fluid-saturated sample (Fig. 7). It reproduced well the laboratory measurements.

Reproducing numerically the transient fluid pressure measured in the laboratory indicates that energy loss due to fluid flow on the mesoscopic scale was similar in both numerical and laboratory experiments. Such attenuation due to fluid flow on the mesoscopic scale, added to frame-related attenuation, was enough to reproduce attenuation measured in the laboratory. These results allow inferring that wave-induced fluid flow on the mesoscopic scale and matrix anelasticity are the dominant mechanisms for seismic attenuation in partially saturated sandstone.

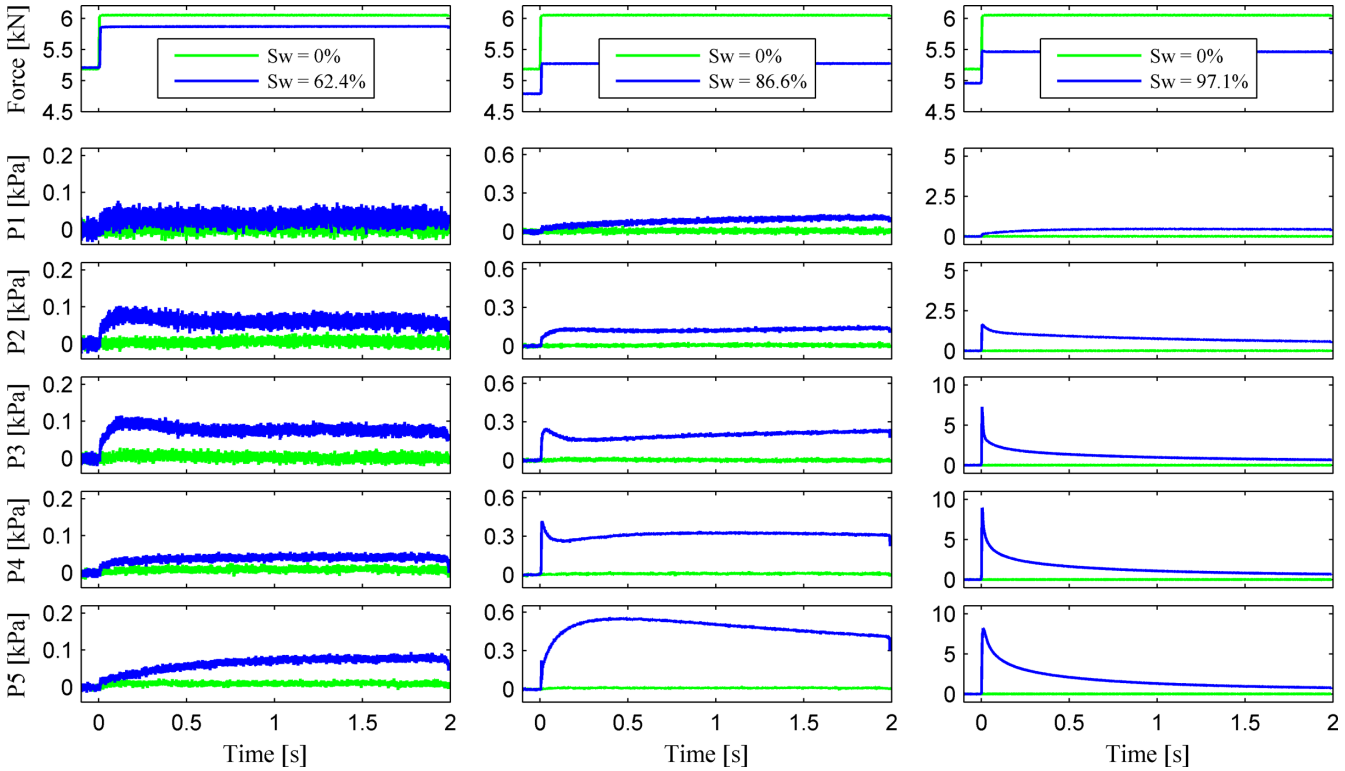

Figure 3. Laboratory measurements of fluid pressure along the sample (positions indicated in Fig. 1) and the respective step forces that were applied on top of the sample. The data shown are for Berea sandstone in four conditions: dry (green curves repeated in all the plots), 62.4, 86.6 and 97.1 per cent water (blue curves in the columns on the left, middle and right). The signal looks noisier in the plots on the left because of the different scales of the *y*-axes.

DISCUSSION

The transient fluid pressure measured in the lower part of the sample saturated with 97.1 per cent water is about one order of magnitude higher than in the sample saturated with 86.6 per cent water (Fig. 3). This is due to a significantly reduced presence of air in the lower part of the sample saturated with 97.1 per cent water. This reduction in air saturation was achieved through a long period of pumping (about 20 hr for 97.1 per cent water and 1–2 hr for 86.6 per cent water). On the other hand, the measurements of attenuation are relatively similar for samples saturated with 86.6 and 97.1 per cent water (Fig. 2), which are higher than for the sample saturated with 62.4 per cent water. Murphy (1982a) observed a similar behaviour for water-saturated Massilon sandstone: attenuation starts to increase for saturation around 60 per cent, reaches a maximum around 80 per cent and then, it decreases approaching fully saturated conditions.

The measurements of Young's modulus result in values of about 12 GPa for dry and about 7 GPa for partially saturated samples (Fig. 2). Looking at data measured for saturations below 60 per cent (not shown here), we observed that a significant increase of the Young's modulus occurs below about 10 per cent water saturation. This effect has been commonly observed and is reported by, for example, Murphy (1982b), Knight & Dvorkin (1992), Tutuncu (1992) and Cadoret (1993). Mavko *et al.* (2009) summarize their discussions by stating that, for the first few percent of water saturation, a decrease in the Young's modulus with increasing water saturation has been attributed to softening of cements (sometimes called chemical weakening), to clay swelling and to surface effects.

While approximately constant attenuation in dry rocks can be mainly attributed to friction between grains and/or crack boundaries (Walsh 1966; Nowick & Berry 1972; Johnston *et al.* 1979), frequency-dependent attenuation is mainly due to fluid flow in the saturated case (White 1975; Mavko & Jizba 1991; Pride *et al.* 2004). Therefore, we employed two phenomenological models, the Nearly Constant Q (NCQ) model (Liu *et al.* 1976) and the standard linear solid (SLS) model (Carcione 2007) to fit the laboratory data (Fig. 2). The data [Re(E) and Q^{-1}] for the dry sample were successfully fit using only the NCQ model while the data for the saturated sample were fit using an arithmetic superposition of these two models (Appendix C).

Johnston *et al.* (1979) assumed that the frequency-independent and frequency-dependent attenuation mechanisms were independent and that those taking place in dry rocks also take place in saturated rocks. Measurements on dry and partially saturated rocks suggested that the frequency-independent component was due to matrix anelasticity and the frequency-dependent component was related to the fluid saturation. Matrix anelasticity includes the intrinsic (1) attenuation of matrix minerals and (2) aggregate minerals, in addition to (3) frictional dissipation due to relative motions at the grain boundaries and across crack surfaces (Walsh 1966; Johnston *et al.* 1979). The intrinsic attenuation of minerals is generally small ($Q^{-1} < 0.001$, Nowick & Berry 1972), while in the whole rock attenuation is normally much higher ($Q^{-1} \sim 0.01$, Barton 2007). In our dry sample, Q^{-1} is about 0.015 at room conditions (Fig. 2). According to Walsh (1966), friction is probably the major factor under these conditions. Residual water (at least a mono-molecular layer) remains in grain boundaries and thin cracks and lubricates their surfaces. This favours sliding motions to take place even for low strains of the order 10^{-6}, as in our laboratory experiments. Attenuation is much lower in water absent rock (e.g. Tittmann *et al.* 1975) because sliding is more difficult (Johnston *et al.* 1979).

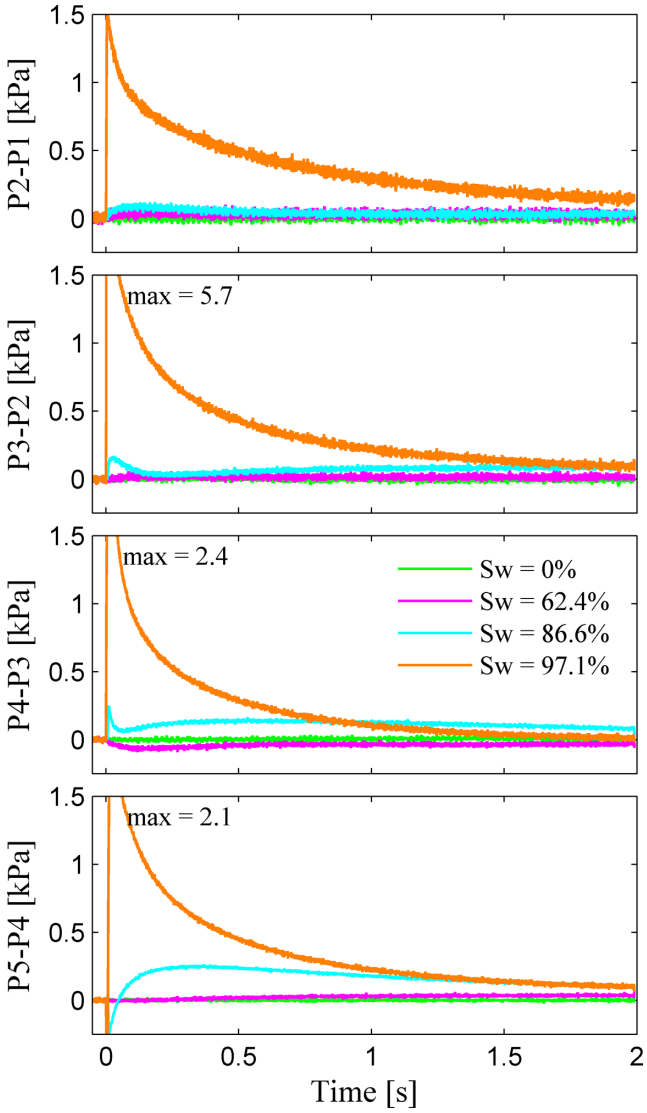

Figure 4. Pressure differences between neighbour sensors (Fig. 1) along the sample in four saturation conditions: dry, 62.4, 86.6 and 97.1 per cent water. For convenience, in the three lower plots, the maxima of the curves for 97.1 per cent water saturation are out of the plot limits but their values are indicated as 'max'.

Another case in which attenuation due to friction becomes negligible is when the rock is subjected to confining pressures high enough to close all cracks (Walsh 1966).

Our interpretation for the frequency-dependent fluid-related attenuation is different than that of Johnston *et al.* (1979) because we study attenuation in a frequency range where a different mechanism dominates. Johnston *et al.* (1979) concluded that Biot-type fluid flow mechanism (Biot 1962), although not necessarily dominating, plays an important role in the overall attenuation. However, at seismic frequencies, attenuation due to this mechanism is negligible for usual properties of fluid-saturated rocks (Bourbié *et al.* 1987). We showed that the frequency-dependent component of our laboratory data can be explained with wave-induced fluid flow on the mesoscopic scale. If this mechanism, together with matrix anelasticity, is responsible for high values of attenuation ($Q^{-1} \sim 0.06$) at seismic frequencies, its occurrence in subsurface porous rocks partially saturated with hydrocarbons (or other fluids) should be further investigated (e.g. Quintal 2012; Quintal *et al.* 2012; Rubino & Holliger 2012).

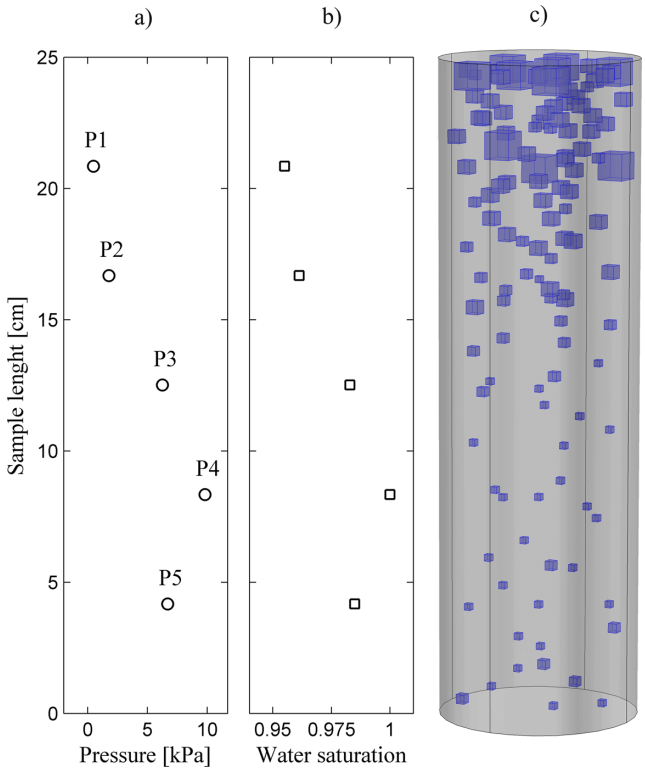

Figure 5. (a) Values of fluid pressure measured in the laboratory at a time very close to zero (from curves in Fig. 3) at the five locations in the sample. (b) Water saturation calculated as a linear function of the fluid pressure values showed in (a). (c) Numerical model having a background fully saturated with water and cubic patches fully saturated with air, resulting in an overall saturation of 98 per cent water.

The measurements for attenuation and fluid pressure (Figs 2 and 3) were performed at different strains (Table 2). Thus, we performed an additional series of measurements to check how this difference influences results. We measured transient fluid pressure at several strains for the sample saturated with 97.1 per cent water (Fig. 8). The fluid pressure increased linearly with strain at the same rate for different times. This indicates that the fluid flow pattern must be the independent of strain and, therefore, fluid-related attenuation.

We roughly estimate the fluid pressure resulting from the vertical strain to understand the stress–strain condition that the saturating fluids undergo in the laboratory experiments. According to the definition of compressibility (Jaeger *et al.* 2007), fluid pressure is given by:

$$P_{\mathrm{f}} = \frac{K_{\mathrm{fl}}\varepsilon_v}{\phi}, \tag{7}$$

where ϕ is porosity (20 per cent, Table 1), K_{fl} is the bulk modulus of the effective single-phase fluid and ε_v is the total sample volumetric strain caused by the step stress,

$$\varepsilon_v = 1 - \frac{1}{(1+\varepsilon\nu)^2\,(1-\varepsilon)}, \tag{8}$$

ε is the vertical strain ($\varepsilon = 2 \times 10^{-5}$, Table 2), and ν is the Poisson's ratio (Mavko *et al.* 2009). We consider a Poisson's ratio ranging between 0.15 and 0.3 (Zimmerman 1991). The upper and lower limits of pressure that the fluids might experience are defined by

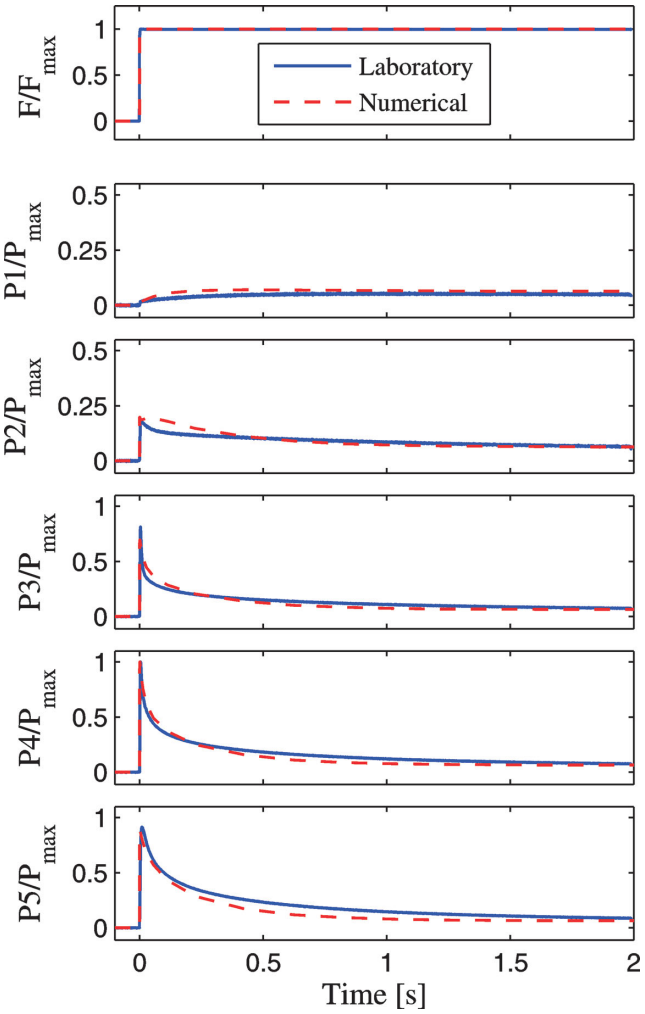

Figure 6. Laboratory measurements of fluid pressure (from Fig. 3) and numerical results for the model shown in Fig. 5(c). The step force that was applied on top of the numerical model is shown on the top plot.

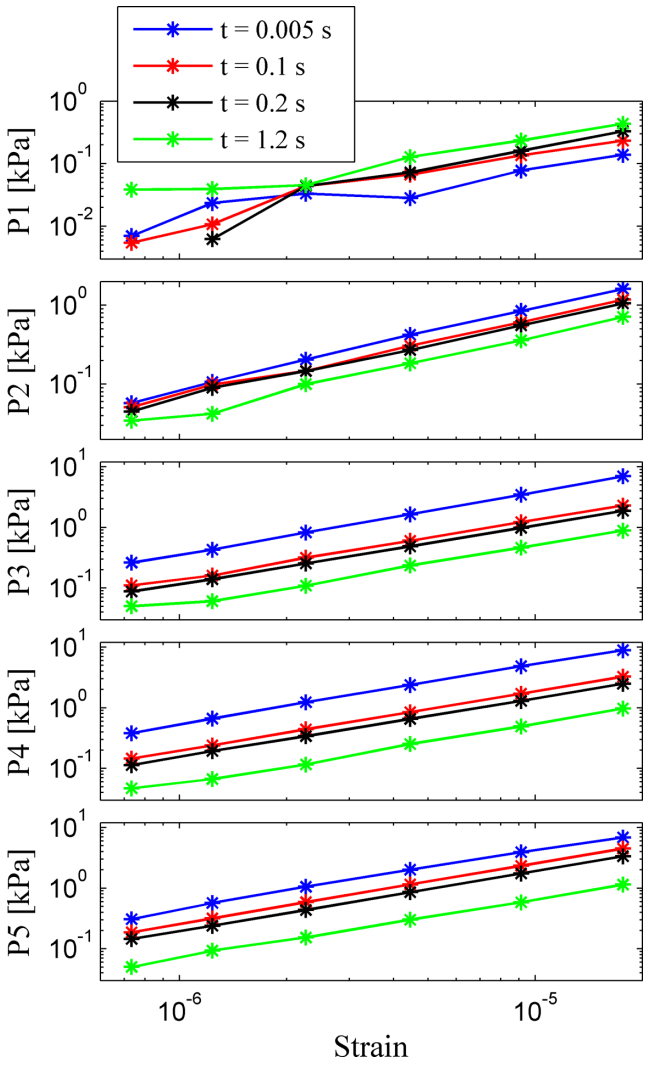

Figure 8. Laboratory measurements of fluid pressure in the five locations indicated in Fig. 1, at different times, versus vertical strain. The sample was saturated with 97.1 per cent water.

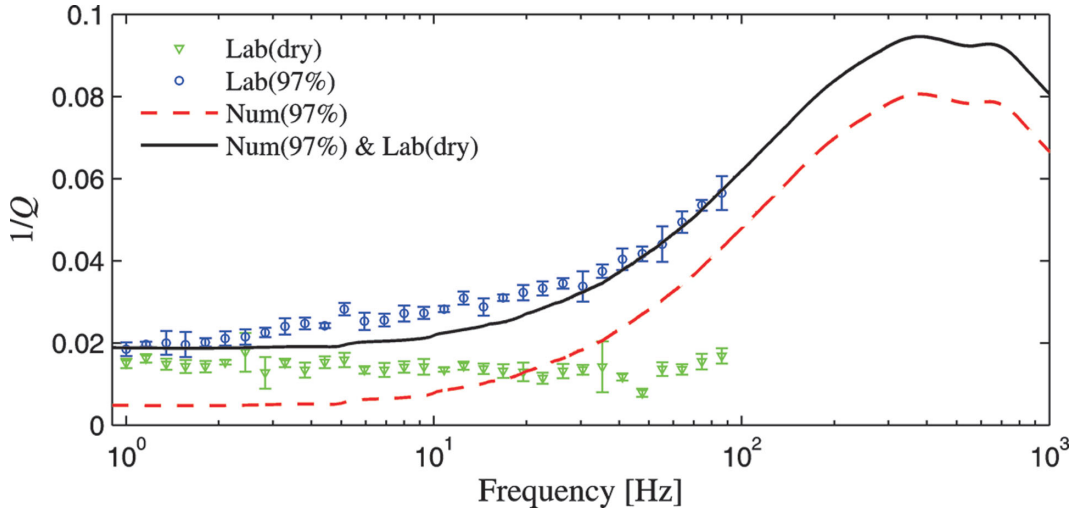

Figure 7. Laboratory measurements of attenuation for the sample in dry condition and saturated with 97.1 per cent water (from Fig. 1), denoted 'Lab(dry)' and 'Lab(97.1 %)'. Numerical results for attenuation due to wave-induced fluid flow using the numerical model shown in Fig. 5c, denoted 'Num(97.1 %)'. The curve denoted 'Num(97.1 %) & Lab(dry)' results from summing the numerically calculated attenuation to the mean value of attenuation measured in the dry sample.

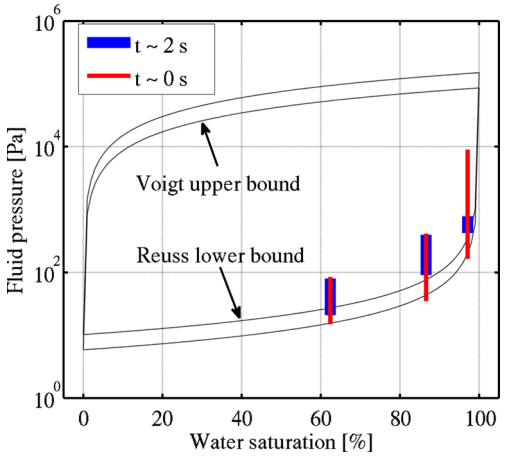

Figure 9. Interval (minimum to maximum) fluid pressure measured at times $t \to 0$ s and $t = 2$ s (shown as red and blue bars), compared with the predicted fluid pressure (black curves), as a consequence of a vertical strain of 2×10^{-5}, according to the two bounds (Voigt and the Reuss) for the effective bulk modulus of the fluid. The double lines for each bound are confidence lines calculated considering a variation of the Poisson's ratio between 0.15 and 0.3.

using the Voigt (isostrain) and Reuss (isostress) averaging rules, respectively, for K_{fl} in eq. (7):

$$K_{\text{fl[Voigt]}} = \sum_{i=1}^{n} S_i K_i, \tag{9}$$

$$\frac{1}{K_{\text{fl[Reuss]}}} = \sum_{i=1}^{n} \frac{S_i}{K_i} \tag{10}$$

(Mavko *et al.* 2009), where S_i is the saturation of the i-th phase and K_i is the bulk modulus of the i-th phase (Table 3). We compare the theoretical limits with intervals of fluid pressure observed in our data (Fig. 9). These intervals are defined by the minimum and maximum values of fluid pressure for 62.4, 86.6 and 97.1 per cent water saturation degrees. These minimum and maximum values are picked at times $t \sim 2$ s and $t \sim 0$, respectively. We observe that the intervals are located between the two limits, but much closer to the Reuss lower bound. Voigt and Reuss limits are associated with the high- and low-frequency limits, respectively, of the attenuation mechanism accounted for in our numerical results. This is in agreement with our numerical results, since the laboratory data correspond to the low-frequency side of the attenuation peak in the numerical curve (Fig. 7).

CONCLUSIONS

We performed laboratory measurements of seismic attenuation and transient fluid pressure in a partially saturated Berea sandstone sample at room pressure and temperature. Combining these measurements is a new methodology to investigate fluid-related attenuation in rocks. The laboratory results suggested that wave-induced fluid flow on the mesoscopic scale is one of the dominant mechanisms responsible for attenuation in partially saturated sandstone.

Numerical modelling was done to assist in the interpretation of laboratory data. We used a poroelastic model that represented the 97.1 per cent water-saturated sample used in the laboratory. Transient fluid pressure computed in this model was equivalent to that measured in the laboratory and was associated with fluid flow on the mesoscopic scale. The numerical results for attenuation, uniquely due to fluid flow, added to a frequency-independent attenuation due to the solid frame, reproduced well the laboratory data. This confirmed that wave-induced fluid flow on the mesoscopic scale is the dominant mechanism for the frequency-dependent component of seismic attenuation in partially saturated sandstone.

ACKNOWLEDGEMENTS

We thank Jean-Pierre Burg for the internal review. Claudio Madonna and Brad Artman contributed to the laboratory experimental design, while Robert Hofmann and Reto Seifert solved many technical issues. Holger Steeb contributed with many enlightening discussions. Luigi Burlini initiated this project but sadly passed at an early stage of the research. This work was partially supported by the CTI (Swiss Commission for Technology and Innovation) and the LFSP (Low Frequency Seismic Partnership).

REFERENCES

Barton, N., 2007. *Rock Quality, Seismic Velocity, Attenuation and Anisotropy,* Taylor & Francis.

Batzle, M.L., Han, D.-H. & Hofmann, R., 2006. Fluid mobility and frequency-dependent seismic velocity: direct measurements, *Geophysics,* **71,** N1–N9.

Berryman, J.G., 1999. Origin of Gassmann's equations, *Geophysics,* **64,** 1627–1629.

Biot, M.A., 1941. General theory of three-dimensional consolidation, *J. appl. Phys.,* **12,** 155–164.

Biot, M.A., 1962. Mechanics of deformation and acoustic propagation in porous media, *J. appl. Phys.,* **33,** 1482–1498.

Bourbié, T., Coussy, O. & Zinszner, B., 1987. *Acoustics of Porous Media,* Editions Technip, Paris.

Cadoret, T., 1993. Effet de la saturation eau/gaz sur les propriétés acoustiques des roches, *PhD dissertation*, University of Paris VII, Paris.

Carcione, J.M., 2007. *Wave Fields in Real Media: Wave Propagation in Anisotropic, Anelastic, Porous and Electromagnetic Media*, Elsevier Science.

Dunn, K.-J. 1986. Acoustic attenuation in fluid-saturated porous cylinders at low frequencies, *J. acoust. Soc. Am.,* **79**(6), 1709–1721.

Dutta, N.C. & Odé, H., 1979a. Attenuation and dispersion of compressional waves in fluid filled porous rocks with partial gas saturation (White model)—part I: results, *Geophysics,* **44,** 1777–1788.

Dutta, N.C. & Odé, H., 1979b. Attenuation and dispersion of compressional waves in fluid filled porous rocks with partial gas saturation (White model)—part II: results, *Geophysics,* **44,** 1789–1805.

Gardner, G.H.F., 1962. Extensional waves in fluid-saturated porous cylinders, *J. acoust. Soc. Am.,* **34**(1), 36–40.

Gassmann, F., 1951. Über die Elastizität poröser Medien: Vierteljahreschrift der Naturforschenden Gesellschaft in Zürich, **96,** 1–23.

Jaeger, J.C., Cook, N.G.W. & Zimmerman, R.W., 2007. *Fundamentals of Rock Mechanics,* 4th edn, Blackwell Pub.

Johnston, D.H., Toksoz, M.N. & Timur, A., 1979. Attenuation of seismic wave in dry and saturated rocks: II. Mechanisms, *Geophysics,* **44,** 691–711.

Knight, R. & Dvorkin, J., 1992. Seismic and electrial properties of sandstones at low saturations, *J. geophys. Res.,* **97,** 17 425–17 432.

Lakes, R., 2009. *Viscoelastic Materials,* Cambridge University Press.

Liu, H.-P., Anderson, D.L. & Kanamori, H., 1976. Velocity dispersion due to anelasticityL implications for seismology and mantle composition, *Geophys. J. Int.,* **47,** 41–58.

Madonna, C. & Tisato, N., 2013. A new seismic wave attenuation module to experimentally measure low-frequency attenuation in extensional mode, *Geophys. Prospect.,* **61,** 302–314.

Madonna, C., Almqvist, B.S.G. & Saenger, E.H., 2012. Digital rock physics: numerical prediction of pressure-dependent ultrasonic velocities using micro-CT imaging, *Geophys. J. Int.,* **189,** 1475–1482.

Masson, Y.J. & Pride, S.R., 2007. Poroelastic finite-difference modeling of seismic attenuation and dispersion due to mesoscopic-scale heterogeneity, *J. geophys. Res.,* **112,** B03204, doi:10.1029/2006JB004592.

Mavko, G. & Jizba, D., 1991. Estimating grain-scale fluid effects on velocity dispersion in rocks, *Geophysics,* **56,** 1940–1949.

Mavko, G., Mukerji, T. & Dvorkin, J., 2009. *The Rock Physics Handbook: Tools for Seismic Analysis of Porous Media,* 2nd edn, Cambridge University Press.

McKavanagh, B. & Stacey, F.D., 1974. Mechanical hysteresis in rocks at low strain amplitudes and seismic frequencies, *Phys. Earth planet. Inter.,* **8,** 246–250.

Mitchell, B.J. & Romanowicz, B.A., 1999. *Q of the Earth: Global, Regional, and Laboratory Studies, Pageoph Topical Volumes,* Birkhäuser Verlag.

Murphy, W.F. III, 1982a. Effects of partial water saturation on attenuation in Massilon sandstone and Vycor porous glass, *J. acoust. Soc. Am.,* **71**(6), 1458–1468.

Murphy, W.F. III, 1982b. Effects of microstructure and pore fluids on the acoustic properties of granular sedimentary materials, *PhD dissertation*, Stanford University, Palo Alto.

Nowick, A.S. & Berry, B.S., 1972. *Anelastic Relaxation in Crystalline Solids,* Academic Press.

Paffenholz, J. & Burkhardt, H., 1989. Absorption and modulus measurements in the seismic frequency and strain range on partially saturated sedimentary rocks, *J. geophys. Res.,* **94**(B7), 9493–9507.

Pride, S.R., Berryman, J.G. & Harris, J.M., 2004. Seismic attenuation due to wave-induced flow, *J. geophys. Res.,* **109,** B01201, doi:10.1029/2003JB002639.

Quintal, B., 2012. Frequency-dependent attenuation as a potential indicator of oil saturation, *J. appl. Geophys.,* **82,** 119–128.

Quintal, B., Steeb, H., Frehner, M. & Schmalholz, S.M., 2011. Quasi-static finite element modeling of seismic attenuation and dispersion due to wave-induced fluid flow in poroelastic media, *J. geophys. Res.,* **116,** B01201, doi:10.1029/2010JB007475.

Quintal, B., Steeb, H., Frehner, M., Schmalholz, S.M. & Saenger, E.H., 2012. Pore fluid effects on S-wave attenuation caused by wave-induced fluid flow, *Geophysics,* **77,** L13–L23.

Rubino, J.G. & Holliger, K., 2012. Seismic attenuation and velocity dispersion in heterogeneous partially saturated porous rocks, *Geophys. J. Int.,* **188,** 1088–1102.

Rubino, J.G., Ravazzoli, C.L. & Santos, J.E., 2009. Equivalent viscoelastic solids for heterogeneous fluid-saturated porous rocks, *Geophysics,* **74,** N1–N13.

Spencer, J.W. Jr., 1981. Stress relaxations at low frequencies in fluid-saturated rocks: attenuation and modulus dispersion, *J. Geophys. Res.,* **86**(B3), 1803–1812.

Tisato, N. & Madonna, C., 2012. Attenuation at low seismic frequencies in partially saturated rocks: measurements and description of a new apparatus, *J. appl. Geophys.,* **86,** 44–53.

Tittmann, R.B., Houseley, R.M. & Abdel-Gawad, M., 1975. Internal friction quality factor ≥3100 achieved in lunar rock 70215, 85, *Abstr. Lunar planet. Sci. Conf.,* **6,** 812–814.

Tutuncu, A.N., 1992. Velocity dispersion and attenuation of acoustic waves in granular sedimentary media, *PhD dissertation*, University of Texas, Austin.

Walsh, J.B., 1966. Seismic wave attenuation in rock due to friction, *J. geophys. Res.,* **71,** 2591–2599.

Wang, H.F., 2000. *Theory of Linear Poroelasticity with Applications to Geomechanics and Hydrogeology,* Princeton University Press.

Wenzlau, F., Altmann, J.B. & Müller, T.M., 2010. Anisotropic dispersion and attenuation due to wave-induced fluid flow: quasi-static finite element modeling in poroelastic solids, *J. geophys. Res.,* **115,** B07204, doi:10.1029/2009JB006644.

White, J.E., 1975. Computed seismic speeds and attenuation in rocks with partial gas saturation, *Geophysics,* **40,** 224–232.

Yin, C.-S., Batzle, M.L. & Smith, B.J., 1992. Effects of partial liquid/gas saturation on extensional wave attenuation in Berea sandstone, *Geophys. Res. Lett.,* **19**(13), 1399–1402.

Zienkiewicz, O.C., Chan, A.H.C., Pastor, M., Schrefler, B.A. & Shiomi, T., 1999. *Computational Geomechanics with Special Reference to Earthquake Engineering,* John Wiley.

Zimmerman, R.W., 1991. *Compressibility of Sandstones,* Developments in Petroleum Science 29, Elsevier.

APPENDIX A: SAMPLE SEALING

Before placing the sample in the BBAV, an aluminum foil was glued onto the curved surface of the sample. The sample is isolated from the confining medium (air) by means of a fluorinated ethylene propylene (FEP) shrink-tube (jacket). Glued aluminum foil and the jacket did not increase the stiffness of the sample and avoided that a free-flow boundary was applied to the specimen. In fact, this multilayer seal impedes that the saturating fluid escapes radially from the sample while it is vertically stressed (Gardner 1962; Dunn 1986; Yin *et al.* 1992).

APPENDIX B: FLUID PRESSURE SENSORS

To introduce the sensors into the sample, we drilled on the side of the specimen five holes, 3.8 cm long and 4.2 cm vertically apart from each other (Fig. 1). The diameter of these holes was 0.5 cm in the first 3.5 cm and 0.3 cm in the last 0.3 cm. Free space between the rigid body of the sensor and the inner wall of the placing hole was reduced by inserting the sensor in a 0.5 by 0.3 cm diameter latex pipe (Fig. 1). Free space causes artificial porosity which would change significantly the properties of our rock sample and could host air during the experiments. Because air is much more compressible than liquids (Table 3), its presence around the sensors would bias the signal measured. A clip, made of brass, was applied near to the sensor-end on the latex pipe to seal the sensor from the inner wall of the latex pipe. The extremity of the latex pipe on the side of the external surface of the sample was then not sealed and hydraulically connected to the confining fluid. In this condition the confining medium would invade the sample flowing between the external wall of the latex pipe and the internal wall of the hole making impossible the measurements. Thus, a brass cone was pushed against the inner wall of the latex pipe and a plastic ring glued on the sample jacket (Fig. 1). As soon the confining pressure is increased, the latex pipe inflates and adheres to the inner wall of the placing hole reducing the free space.

The fluid pressure sensors (3L_10L_g-1, Keller AG, Winterthur, Switzerland) are of 3 mm diameter located on the extremity of a sealed electric cable. They were differential sensors with 200 kPa full-scale. Their sensitive element laid on the sample axis, that is, on the end of each placing hole. We utilized 'zero volume pressure sensors' because they do not have internal dead volume and they allow measuring the pore pressure variation in less than 50 μs. The acquisition rate was 4 kHz allowing the recognition of a variation of fluid pressure as fast as 0.5 ms.

APPENDIX C: FITTING DATA FOR Q^{-1} AND Re(E)

Because the data for Q^{-1} of the dry sample are frequency independent (Fig. 2), they can be approximated with a NCQ model. First we

use $\omega_0 = 2\pi$ rad s^{-1} ($f_0 = 1$ Hz) to interpolate the measured Re(E) for the dry sample with the following regression formula:

$$\mathrm{Re}(E_{\mathrm{NCQ}}) = a \log_{10}(\omega) + \mathrm{Re}(E_{\omega_0}), \tag{C1}$$

where a is the best-fit parameter, ω_0 is the reference angular frequency and Re(E_{ω_0}) is the real part of the Young's modulus at ω_0. The NCQ model allows calculating Q^{-1}_{NCQ} as a function of Re(E_{NCQ}) as:

$$Q^{-1}_{\mathrm{NCQ}} = \left(\sqrt{\frac{\mathrm{Re}\,(E)}{\mathrm{Re}\left(E_{\omega_0}\right)}} - 1 \right) \frac{\pi}{\log\left(\omega / \omega_0\right)}, \tag{C2}$$

which fits well our data, with a standard deviation between Q^{-1}_{NCQ} and the measured Q^{-1} for the dry sample of 0.0023. The interpolation Re(E_{NCQ}) and Q^{-1}_{NCQ} are shown in Fig. 2 together with the measurements for the dry sample.

The attenuation measurements for 62.4, 86.6 and 97.1 per cent water saturation (Fig. 2) are frequency dependent, so they cannot be simply fit with an NCQ model. However, as a first step, we calculate Re(E_{NCQ}) and Q^{-1}_{NCQ} using the NCQ model (eqs C1 and C2). In this case, Q^{-1}_{NCQ} gives the minimum value of our measured frequency-dependent Q^{-1}. Further, the frequency-dependent dispersion, Re(ΔE_{SLS}), was fitted with a SLS model as:

$$\Delta E_{\mathrm{SLS}} = E_{\omega_0} \left(\frac{1 + \mathrm{i}\omega t_0}{1 + \mathrm{i}\omega t_d} - 1 \right), \tag{C3}$$

where and t_0 and t_{d} are the best-fit parameters which define the relaxation times of the SLS model (Carcione 2007; Mavko *et al.* 2009). The real part of Young's modulus Re(E_{fit}) was computed as the sum of the Re(E_{NCQ}) and the dispersion caused by the SLS Re(ΔE_{SLS}):

$$\mathrm{Re}(E_{\mathrm{fit}}) = \mathrm{Re}(E_{\mathrm{NCQ}}) + \mathrm{Re}(\Delta E_{\mathrm{SLS}}). \tag{C4}$$

According to the Kramers–Kronig relation (e.g. Lakes 2009), the attenuation generated by the SLS model characterized by the relaxation times t_0 and t_{d} are calculated with:

$$Q^{-1}_{\mathrm{SLS}} = \frac{\omega(t_0 - t_d)}{1 + \omega^2 t_0 t_d} \tag{C5}$$

(Carcione 2007). Finally, the total attenuation that fits our frequency-dependent data (Q^{-1}_{total}) can be calculated according to Johnston *et al.* (1979):

$$Q^{-1}_{\mathrm{total}} = Q^{-1}_{\mathrm{NCQ}} + Q^{-1}_{\mathrm{SLS}}. \tag{C6}$$

This estimate fits well our data, with standard deviations between the measured Q^{-1} and Q^{-1}_{total}, for 62.4, 86.6 and 97.1 per cent water saturation of 0.0018, 0.0015 and 0.0021, respectively. Such good fits to the measured Q^{-1}, calculated as functions of Re(E), show that our datasets for Re(E) and Q^{-1} obey the causality principle on which the Kramers–Kronig relations is based.